## nature physics

Article

https://doi.org/10.1038/s41567-025-03056-8

# Terahertz excitation of collective dynamics of polar skyrmions over a broad temperature range

Received: 15 February 2024

Accepted: 2 September 2025

Published online: 03 October 2025



Check for updates

Wei Li¹, Sixu Wang¹, Pai Peng², Haojie Han¹, Xinbo Wang ®²⊠, Jing Ma ®¹, Jianlin Luo<sup>2</sup>, Jun-Ming Liu **®** <sup>4</sup>, Jing-Feng Li **®** <sup>1</sup>, Ce-Wen Nan **®** <sup>1</sup> & Qian Li **®** <sup>1</sup> ⊠

Ultrafast coherent control of electric dipoles using terahertz pulses provides a means to discover hidden phases of materials and potentially leads to applications in high-speed optoelectronic devices. Although this approach has been shown to be effective in incipient ferroelectrics only close to the phase transition temperatures, it relies on the soft phonon modes overlapping with the terahertz pulse bandwidth. Because of their emergent subterahertz collective dynamics, a fundamentally distinct and effective terahertz coupling mechanism can be envisaged in topological polar structures in PbTiO<sub>3</sub>/SrTiO<sub>3</sub> superlattices. Here we demonstrate that polar skyrmions can be coherently driven into a hidden phase with transient macroscopic polarization, as probed using terahertz field-induced second-harmonic generation and optical Kerr effects. This ultrafast terahertz-driven phase transition is found to sustain across a broad temperature range of 4–470 K in a corresponding electric field required for equilibrium stability of skyrmions. Dynamical phase-field simulations reveal the correlation between the relaxation behaviour of the excited collective modes and the emergence of the polar phases. Our results manifest dynamical properties of topological polar structures, which could be technologically implemented given their flexibility in structure design and tunability under external electric fields.

In epitaxial ferroelectric/dielectric superlattices, as exemplified by the  $(PbTiO_3)_m/(SrTiO_3)_n$  (m, n are numbers of the unit-cell layer) system, precise tuning of the layer thickness and substrate mismatch strain has been discovered to stabilize nanoscale topological phases with non-collinear polarization vector configurations and long-range in-plane ordered states<sup>1-6</sup>. These exotic phases, such as polar vortex, skyrmion and dipole wave, mainly reside in the constituent ferroelectric layers and exhibit a series of fascinating phenomena rarely seen in conventional ferroelectric materials, including negative capacitance<sup>7,8</sup>,

optical chirality<sup>9-12</sup> and a light-induced supercrystal phase<sup>13,14</sup>. However, compared with their magnetic counterparts<sup>15</sup>, the dynamical behaviours of polar topological phases are yet to be systematically explored to unveil emerging functional properties<sup>16-19</sup>. Microscopy studies have examined the in-situ polarization evolution processes of the polar vortices and skyrmions, revealing their transitions into different topologies or topologically trivial phases under the action of external electric, mechanical or thermal fields<sup>20-25</sup>. Ultrafast diffraction studies have revealed that polar vortices host a set of collective

<sup>1</sup>State Key Laboratory of New Ceramic Materials, School of Materials Science and Engineering, Tsinghua University, Beijing, China. <sup>2</sup>Beijing National Laboratory for Condensed Matter Physics, Institute of Physics, Chinese Academy of Sciences, Beijing, China. 3State Key Laboratory of Low Dimensional Quantum Physics, Department of Physics, Tsinghua University, Beijing, China. 4Laboratory of Solid State Microstructures and Innovation Center of Advanced Microstructures, Nanjing University, Nanjing, China. Me-mail: xinbowang@iphy.ac.cn; qianli mse@tsinghua.edu.cn

vibrational modes within the subterahertz frequency range, akin to the infrared-active optical phonons of the underlying lattices<sup>26</sup>. Such collective modes provide unusual dielectric resonance mechanisms that potentially can be harnessed for electrically tunable devices operating at millimetre-wave and terahertz frequencies<sup>27–29</sup>. In addition, the enhanced structural stabilities of these phases, a topological protection attribute, can foster thermally stable macroscopic functional properties with broadened application scopes. This could be particularly relevant for polar skyrmions whose polarization configuration is of stronger three-dimensional characters and better topological phase stability, compared with polar vortices<sup>8,30</sup>. The collective dynamics of the former system has not been addressed thus far.

Ultrafast coherent manipulation of electric dipoles has been demonstrated in architype perovskite ferroelectrics, including SrTiO<sub>3</sub>. KTaO<sub>3</sub> and BaTiO<sub>3</sub>, using single-cycle, strong-field terahertz pulses by means of direct electrostatic coupling effects. In these systems, crucial to an effective coupling is the spectral overlapping between the terahertz pump pulses and their specific lattice phonon modes to thus realize a resonant excitation state  $^{31-37}$ . Phenomenologically, the free-energy functional of ferroelectrics can be described with respect to the soft phonon mode coordinate  $Q_{FF}$  responsible for the polarization order parameters  $^{38}$ . The polarization of PbTiO $_{3}$  arises from the condensation of its Last mode, in which the displacement of Pb<sup>2+</sup> ions is out of phase with those of Ti<sup>4+</sup> and O<sup>2-</sup> ions<sup>39</sup>. Below the Curie temperature, the double-well free-energy landscape posits  $Q_{\rm FF}$  at a specific value corresponding to the equilibrium polarization 40. Upon terahertz excitations, the  $Q_{FF}$  shifts periodically as a function of the external electric field and thereby triggers polarization oscillations. In general, displacive ferroelectrics exhibit strongly temperature-dependent soft-mode dynamics and thus the spectral overlapping with terahertz excitations is confined to the Curie temperature, beyond which the mode frequencies quickly recover<sup>39,41-43</sup>. The long-range dipolar correlation characters also lead to large potential well depths, rendering the switching of  $Q_{FF}$  over the potential barriers unviable for practical terahertz field strengths. Owing to such structural characteristics, a terahertz-induced transient polar phase can be observed below the equilibrium critical temperature of ~36 K in quantum paraelectric SrTiO<sub>3</sub> (refs. 31,44), whereas the polarization in ferroelectric BaTiO<sub>3</sub> alters only by ~10% at room temperature under similar terahertz excitations<sup>34</sup>.

## Simulations of the collective dynamics of polar skyrmions

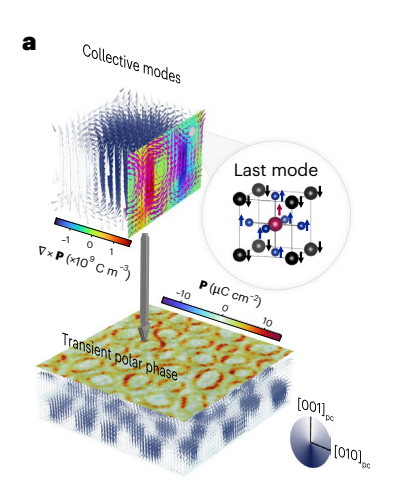
Here we explore single-cycle terahertz pulse-induced ultrafast dynamics of the polar skyrmions stabilized in (PbTiO<sub>3</sub>)<sub>16</sub>/(SrTiO<sub>3</sub>)<sub>16</sub> superlattices. Figure 1a illustrates the schematic of the terahertz excitation phenomena of the system, adapted from the results of dynamical phase-field simulations within the Landau-Ginzburg-Devonshire theory framework (Methods and Extended Data Fig. 1). The system is characterized by the in-plane periodic distribution of individual skyrmions within the PbTiO<sub>3</sub> layers, in between which continuously rotating polarization vectors form the skyrmion walls. Built on the Last phonon mode of PbTiO<sub>3</sub>, multiple collective dynamical modes are hosted in the skyrmions, and their corresponding real-space motions primarily consist of coherent wobbling of the skyrmion walls, accompanied by oscillations of the cores along the out-of-plane direction (Supplementary Video 1). These features are qualitatively similar to the collective modes previously observed in polar vortices<sup>24</sup>. As shown in Fig. 1b, the simulated frequency-domain response spectra indicate a number of well-defined collective modes below ~2 THz, overlapping with the experimental terahertz pulse spectrum (generated by means of the LiNbO<sub>3</sub> optical rectification method). These low-lying collective modes (with mode coordinate  $Q_{Sk}$ ) provide multiple coupling channels with external terahertz electric fields. Compared with architype ferroelectrics, the presence of periodic skyrmion walls weakens the long-range dipole correlation, cancels out the macroscopic polarization<sup>45</sup> and leads to a flattened energy landscape rather than a double-well potential with respect to  $Q_{\rm Sk}=0$  (ref. 7). These factors facilitate the driven motions of  $Q_{\rm Sk}$  into large magnitudes; when  $Q_{\rm Sk}$  gains non-vanishing values, macroscopic symmetry breaking occurs in the skyrmions, leading to the emergence of a transient polar phase (Fig. 1a). In addition, the collective dynamics of the skyrmions marginally shift in frequencies with temperature until a topological phase transition sets in above 500 K (Fig. 1b), which thus provides a remarkable terahertz coupling efficiency across a broad temperature range. These unique dynamical properties are rooted in the topological protection attribute of the skyrmion superlattice, distinct from its components PbTiO<sub>3</sub> and SrTiO<sub>3</sub>.

## Terahertz-induced phase transition in polar skyrmions

To measure the predicted dynamical mechanisms, we performed ultrafast terahertz-pump, second-harmonic generation (SHG) probe and optical Kerr effect probe spectroscopies. As schematically shown in Fig. 2a (see more details in Methods and Extended Data Fig. 2), the terahertz pump and 800-nm probe were collinearly directed onto the sample at normal incidence, with the terahertz electric field oriented along the [100] direction (in the pseudocubic (pc) setting). The 400-nm SHG signals were collected in a near-backscattering direction, sensitive to the terahertz field-induced SHG (TFISH) response arising from the in-plane symmetry breaking 46. The polarization angles of the 800-nm and 400-nm lights (denoted as  $\alpha$  and  $\varphi$ , respectively) were varied relative to the terahertz field direction; for convenience, we define the parallel and perpendicular directions as p- and s-, respectively. The measurements included TFISH polarimetry scans (varying  $\alpha$  and/ or  $\varphi$  angles) at a fixed pump-probe delay time and delay time scans under the p-in/p-out ( $\alpha = \varphi = 0^{\circ}$ ) and s-in/p-out ( $\alpha = 90^{\circ}/\varphi = 0^{\circ}$ ) probing conditions. In addition to skyrmion-hosting (PbTiO<sub>3</sub>)<sub>16</sub>/(SrTiO<sub>3</sub>)<sub>16</sub> superlattices, single c-domain PbTiO<sub>3</sub> thin films and SrTiO<sub>3</sub> single crystals were also investigated as model systems of architype (incipient) ferroelectrics.

Figure 2b presents the time-domain TFISH response spectra of the three systems measured at 300 K. These spectra generally follow the envelope of the squared terahertz waveform, reaching peak responses at a delay time of approximately 0.6 ps; note that the dip in the p-in/p-out spectra of the polar skyrmions at 0.6 ps is due to their oscillatory behaviour (to be discussed later). For PbTiO<sub>3</sub> and SrTiO<sub>3</sub>, large TFISH responses are observed under the p-in/p-out conditions whereas weak to no responses are detected under the s-in/p-out conditions, indicating a pronounced anisotropy. By contrast, the polar skyrmions exhibit comparable TFISH responses in both cases. Further information on the TFISH anisotropy is obtained from the polarimetry patterns measured at the peak delay time. Figure 2c presents the results of the  $\alpha/\varphi$ -coupled scan, equivalent to rotating samples under the  $\alpha = \varphi = 0^{\circ}$  conditions (see  $\alpha$ -scan results in Extended Data Fig. 3a-c). The patterns for PbTiO<sub>3</sub> and SrTiO<sub>3</sub> show similar two-fold symmetries with two lobes parallel to the terahertz electric field. Apart from these two lobes, the patterns for the polar skyrmions manifest an additional set of four lobes and altogether resemble a six-fold-like symmetry. Such six-fold-like patterns are unusual given the pseudocubic crystal symmetry of PbTiO<sub>3</sub>/SrTiO<sub>3</sub> superlattices and suggest complex TFISH mechanisms of the skyrmion system.

Phenomenologically, the TFISH response of materials is the total contribution from the third-order ( $\chi^{(3)}$ ) and second-order ( $\chi^{(2)}$ ) optical nonlinearities, mediated by three mechanisms: four-wave mixing (FWM), hyper-Raman scattering (HRS) and SHG<sup>47–49</sup> (Fig. 2d). FWM is a three-photon process involving two probe photons and one terahertz pump photon, generating a photon at  $2\omega_{\text{probe}}\pm\omega_{\text{THz}}$ . HRS refers to the interaction between the probe light and a material's phonon, generating a photon at  $2\omega_{\text{probe}}\pm\omega_{\text{phonon}}$ . SHG is a two-photon process of the probe light, generating a photon at exactly  $2\omega_{\text{probe}}$ . Both FWM and HRS manifest as sidebands near SHG, but practically are spectrally



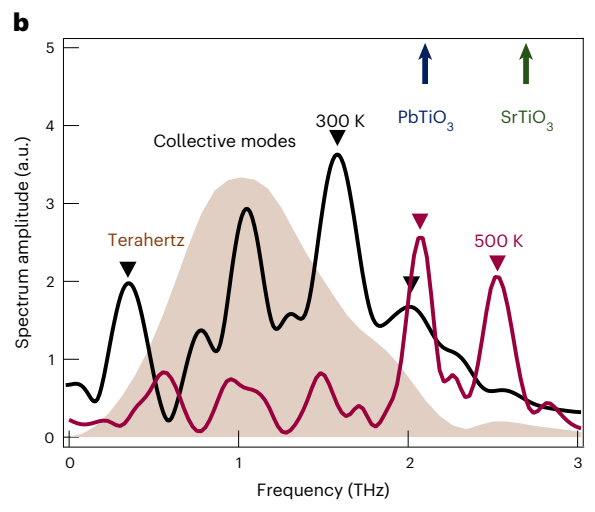


**Fig. 1**| **Simulated collective dynamics of the polar skyrmions. a**, Dynamical phase-field simulation of the collective dynamics of the polar skyrmions in  $(PbTiO_3)_{16}/(SrTiO_3)_{16}$  superlattices. Top left: static configuration of a single skyrmion and the vertical cross-sectional view of the vorticity of the polarization vectors. The arrows denote the motion vectors of ions (pink) or local polarization vectors (white-blue). Top right: schematic of the Last phonon mode in a single unit cell which constitutes the building block of the collective modes. Bottom: excited state of the skyrmions forming a transient polar phase, together

with the horizontal cross-sectional view of the polarization magnitude. **b**, Fourier-transformed spectra of the time-domain polarization response of the polar skyrmions upon terahertz electric field excitation, simulated for 300 K (black) and 500 K (red). The shaded background shows the spectrum of the experimental terahertz pulse. The soft-mode frequencies of SrTiO $_3$  and PbTiO $_3$  at 300 K are indicated with arrows. The triangular symbols denote the positions of the collective modes identified in the spectra.

indistinguishable in TFISH measurements owing to the large bandwidth of femtosecond probe pulses (~30 nm). The FWM response arises from the intrinsic electronic anharmonicities and is not restricted to non-centrosymmetric materials, as confirmed here for all three systems. Their observed TFISH peaks in the p-in/p-out spectra and two-fold polarimetry patterns (Fig. 2b,c) indicate a dominant  $\chi^{(3)}$ response along the terahertz field direction. By contrast, the HRS response only occurs when the material's phonon frequency overlaps with the probe light. Owing to the ineffective coupling of their soft phonons with the terahertz field at 300 K (Fig. 1b), SrTiO<sub>3</sub> and PbTiO<sub>3</sub> exhibit marginal HRS responses, as indicated by the non-oscillatory p-in/p-out TFISH spectra. For both systems, the weak TFISH responses measured under the s-in/p-out conditions (that is, orthogonal to the terahertz field direction) also imply the absence of SHG responses, which is consistent with the fact that paraelectric SrTiO<sub>3</sub> has zero  $\chi^{(2)}$ and the non-zero static  $\chi^{(2)}$  of ferroelectric PbTiO<sub>3</sub> is not detected using the dynamic lock-in method.

The complex TFISH effects observed in the polar skyrmions suggest prominent HRS and SHG contributions. Owing to the effective coupling between their collective modes with the terahertz field, the HRS responses are activated in the polar skyrmions to drive  $Q_{Sk}$  into large amplitudes, consequently breaking the centrosymmetry at equilibrium and inducing a transient polar phase with strong SHG response. The phase-field simulation results (Fig. 2e) indicate that local dipoles become ordered around the skyrmion walls, amounting to a net in-plane polarization along the terahertz field. This terahertz-induced transition is determined by the  $Q_{Sk}$  dynamics, leading to systematic temporal evolutions in the TFISH polarimetry patterns (Extended Data Fig. 3d). Furthermore, we quantify the FWM, HRS and SHG contributions from model fittings to the measured TFISH results (Supplementary Note 1). As shown in Fig. 2f, the fitted  $\chi^{(3)}$  contribution exhibits oscillations overlaid on a fast-decaying slope within ~2 ps. The two  $\chi^{(3)}$  components, FWM and HRS, can be delineated based on the dynamical phase-field simulations (Fig. 2g). The HRS response is derived from the simulated time-dependent mean polarization values, whereas the electronic FWM response is approximated by a Gaussian profile, altogether closely matching the experiment results. The fitted  $\chi^{(2)}$  SHG contribution shows no oscillatory behaviour, which is in line with the transient polar order induced in the system (Extended Data Fig. 3e).

The aforementioned TFISH mechanisms are cross-validated by examining the terahertz field dependence (Extended Data Fig. 4a). Power factors of -2 and -1.75 are found for the p-in/p-out and s-in/p-out responses, respectively. The former power factor agrees with the  $\chi^{(3)}$  contribution, whereas the latter suggests that the  $\chi^{(2)}$  of the terahertz-induced phase is not necessarily proportional to terahertz field.

## Time-domain ultrafast dynamics of polar skyrmions

Next, we focus on the ultrafast dynamics of the polar skyrmions to elucidate the mechanisms of the terahertz-induced polar phase. We incorporated interferometric TFISH (iTFISH) measurements by using a β-BaB<sub>2</sub>O<sub>4</sub> single crystal as a local oscillator, which allows extraction of both the amplitude and phase information with enhanced sensitivities<sup>50</sup> (Methods and Supplementary Note 2). As shown in Fig. 3a, the iTFISH amplitude spectrum features two prominent peaks upon the main terahertz pulse, followed by oscillations over an extended period corresponding to the HRS responses of the collective modes. The iTFISH phase spectrum exhibits several π switching events, which thus reflects changes in the macroscopic polarization direction (Fig. 3a, inset) that flip the signs of the nonlinear susceptibility tensors. These changes are not uniform during the initial ~6-ps period, suggesting a competition between multiple excited collective modes (Fig. 1b). The inherent connection with the collective dynamics underscores viable terahertz control over the macroscopic polar state of the system.

The phase-signed iTFISH signals ( $I_{\mathsf{TFISH}}\cos(\varphi)$ ) provide direct tracing of the  $Q_{\mathsf{Sk}}$  mode coordinates, as shown in Fig. 3b. For comparison, we also measured the terahertz-induced Kerr effect (TKE), which is sensitive to changes in the linear optical susceptibility of the polar skyrmions<sup>51</sup>. Similar to TFISH, the TKE spectrum also shows a large initial electronic response and then a trail of oscillations after the main terahertz pulse. The frequency spectra of these oscillations are obtained from the Fourier transformation of the measured iTFISH and TKE spectra (Fig. 3c). They exhibit three main mode frequencies

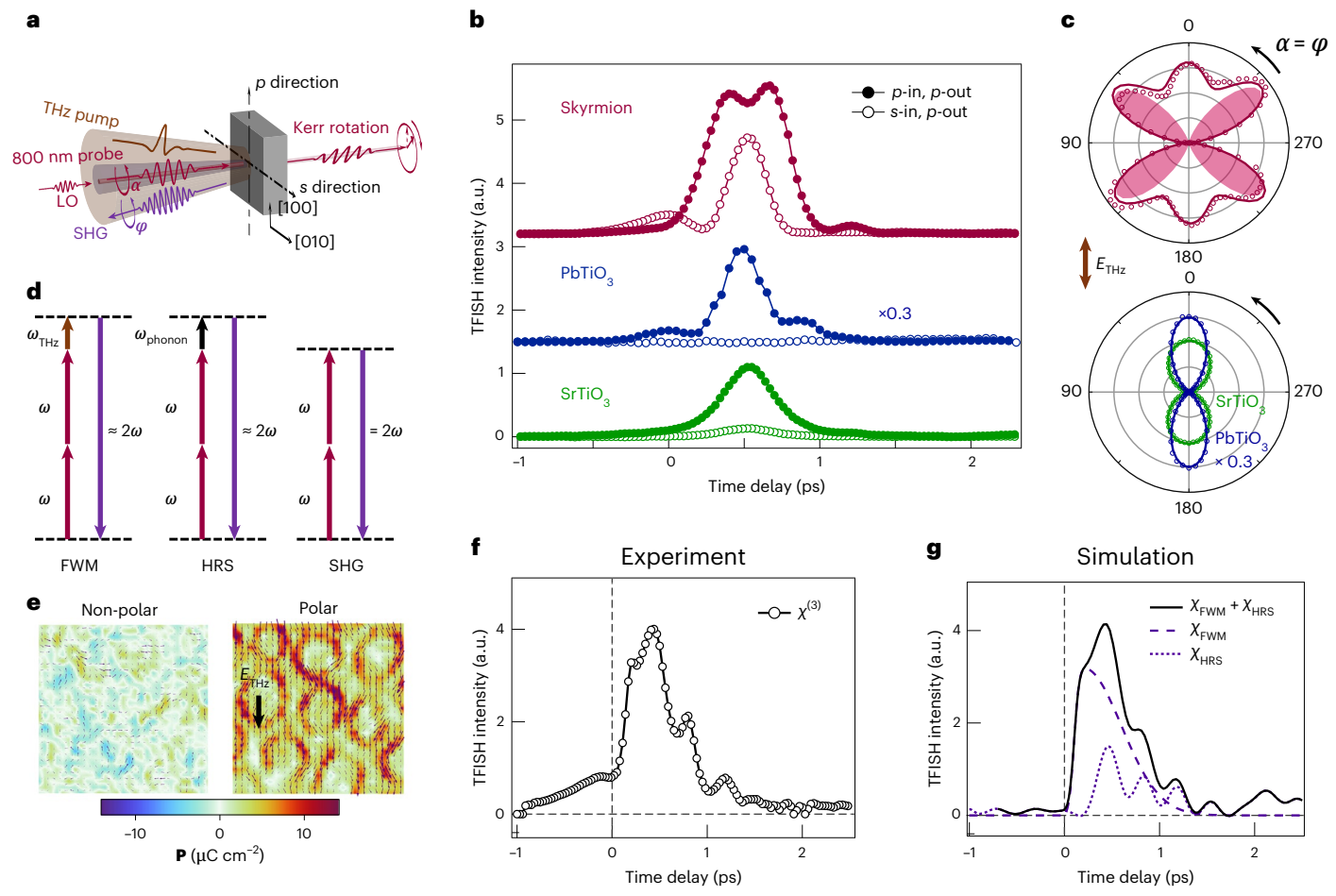


**Fig. 2** | **TFISH in the polar skyrmions. a**, Schematic of the ultrafast terahertz measurement geometry and the definition of the principal axes. **b**, Time-domain TFISH response spectra for the polar skyrmions, PbTiO $_3$  thin films and SrTiO $_3$  single crystals. The p-in/p-out spectrum of PbTiO $_3$  is multiplied by 0.3 for clarity. **c**, TFISH polarimetry plots measured at a delay time of -0.6 ps for the three systems. The  $\chi^{(2)}$  contribution extracted from the model fitting is highlighted by shadowing. **d**, Schematic of the three distinct TFISH mechanisms: FWM, HRS and

SHG. **e**, Spatial distribution of the in-plane polarization of the polar skyrmions before and after the terahertz field excitation, obtained from dynamical phase-field simulations. **f**, Model-fitted  $\chi^{(3)}$  contribution to the p-in/p-out TFISH spectra of the polar skyrmions. **g**, Decomposition of the FWM and HRS responses to the  $\chi^{(3)}$  contribution based on the dynamical phase-field simulations. All the experiment results here were measured at -300 K.

at approximately 0.2 THz, 0.6 THz and 2.1 THz, which is in remarkable agreement with the phase-field simulation results (Fig. 1b). Note that the 0.2 THz mode is observed only in the p-in/p-out TFISH signals, whereas the other modes appear in all three measurements. This difference in mode sensitivity is attributed to the symmetries of the collective modes, determined by their spatial polarization configurations.

The dynamical phase-field simulations further provide real-space microscopic insights into the skyrmion collective modes. Using a frequency decomposition method (Supplementary Note 3), we extracted the spatiotemporal dynamics of local polarization (P) and motion vectors (u) for representative modes. Figure 3d presents schematics of the 0.2 THz and 2.1 THz modes along with the corresponding phase-field simulated patterns (Supplementary Video 2). The collective modes alter the magnitude of the polarization vectors ( $\Delta \mathbf{P}$ ), accompanied by atomic motions  $\Delta \mathbf{u}$  (violet arrows). The 0.2-THz mode exhibits a circular pattern of atomic motions with alternating directions between adjacent skyrmions, thereby producing a temporal oscillation of vorticity  $(\nabla \times \mathbf{u})$ . Notably, this lowest-frequency mode appears to be in-plane symmetric, as the atomic motions cancel out between each pair of the adjacent circular patterns. By contrast, the 2.1-THz mode involves in-plane atomic motions with strong directionality along the terahertz field direction (the [100] crystal axis). This mode breaks the in-plane centrosymmetry, which substantially contributes to both HRS and

SHG responses. Therefore, the 2.1-THz mode is detected under both p-in/p-out and s-in/p-out conditions, whereas the 0.2-THz mode only produces an HRS signal detectable in the p-in/p-out condition. The skyrmion collective modes also exhibit different relaxation behaviours, as indicated by the short-time Fourier transform of the simulated terahertz response (Fig. 3e). The higher-frequency modes decay rapidly within the first 10 ps, in contrast to the 0.2-THz mode which persists throughout the simulated period. This is consistent with the iTFISH results showing a fast relaxation of the oscillatory modes with high frequencies (Fig. 3a). The long-living 0.2-THz mode can be observed up to 80 ps (Extended Data Fig. 5). Altogether, we conclude that although multiple collective modes of the polar skyrmions are excited to form a superimposed state, the fast-decaying higher-frequency modes dominate the emergence of the transient polar phase.

## Temperature-dependent behaviours

The TFISH dynamics of the polar skyrmions exhibits unique temperature evolution behaviours. Figure 4a presents their peak TFISH responses over a wide temperature range of  $\sim$ 4–500 K. The results for PbTiO $_3$  thin films are also included for comparison. Most notably, the TFISH responses of the polar skyrmions, measured under both the p-in/p-out (as has been attributed to the FWM/HRS contributions) and s-in/p-out (the SHG contribution) conditions, undergo an abrupt change at  $\sim$ 470 K reminiscent

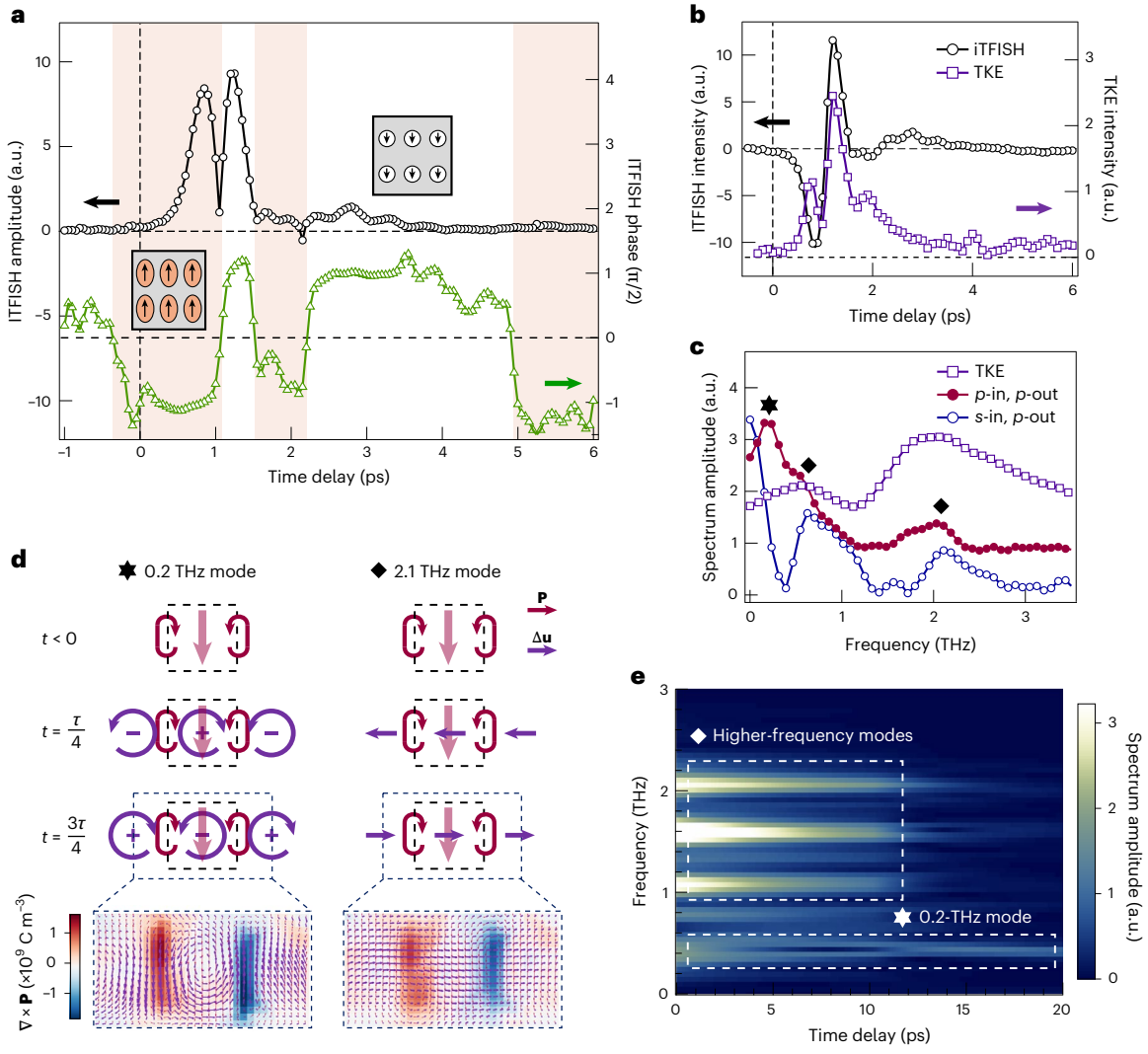


**Fig. 3** | **Terahertz-induced time-domain dynamics of the polar skyrmions. a**, Time-domain spectra of the iTFISH amplitude (black) and phase (green) for the polar skyrmions, extracted from the interferometric measurements under the *p*-in/*p*-out condition. Insets: illustration of the transient dipole ordering. **b**, Time-domain spectra of the phase-signed *p*-in/*p*-out iTFISH (black) and TKE (violet) responses for the polar skyrmions. **c**, Fourier-transformed frequency spectra of the *p*-in/*p*-out iTFISH, *s*-in/*p*-out iTFISH and the TKE measurement results. The hexagram and diamond symbols denote the positions of the collective modes identified in the spectra. **d**, Schematics of the spatial

distributions of local polarization and motion vectors for the representative collective modes of the polar skyrmions. A skyrmion (dashed lines) consists of a quasisingle domain core (light red arrows) surrounded by walls (red arrows) where the polarization vectors rotate around the core. The corresponding phase-field simulated configurations are shown below. Here, t and  $\tau$  denote the time and mode period, respectively.  $\mathbf{e}$ , Short-time Fourier transformation results of the phase-field simulated terahertz-induced response. All the experiment results here were measured at -300 K.

of a first-order phase transition. With increasing temperature until 470 K, the FWM/HRS contribution increases steadily, whereas the SHG contribution shows a moderate decreasing trend with several steps. Except for the overall intensities, the TFISH spectral features appear to be largely unchanged for both probing conditions (Extended Data Fig. 6a,b), corroborating the phase-field results (Fig. 1b). These observations of the polar skyrmions are qualitatively different from those of PbTiO<sub>3</sub>, which essentially exhibits a consistent TFISH response under the p-in/p-out condition within the entire temperature range. The latter trend of PbTiO<sub>3</sub> can be expected given that its ferroelectric phase transition occurs at a much higher temperature (~760 K); for the same reason, its soft-mode frequency remains to lie well beyond the terahertz excitation spectrum, which thus results in a negligible TFISH response under the s-in/p-out condition. In addition, a surge in the (p-in/p-out) TFISH response signifying ferroelectricity is confirmed for SrTiO<sub>3</sub> at 5 K (Fig. 2c), which again contrasts with the polar skyrmions<sup>31</sup>.

The structural transitions of (PbTiO<sub>3</sub>)<sub>16</sub>/(SrTiO<sub>3</sub>)<sub>16</sub> superlattices are revealed by temperature-dependent X-ray diffraction measurements within 300-670 K. As depicted in Fig. 4b, the out-of-plane lattice parameter exhibits a discernible kink around 470 K, and the linear thermal expansion coefficients differ slightly across the transition. Note, however, that such a transition is not accompanied with a complete loss of the in-plane ordered state, as evidenced by the preserved satellite diffraction intensities (Extended Data Fig. 6d). These observations  $corroborate \, the \, TFISH \, results \, and \, suggest \, a \, subtle \, structural \, transition \,$ path of the system, unidentified in previous reports of polar skyrmions. To reveal the likely polarization configurations above 470 K, we simulate the thermal effects by adjusting the substrate strain and Landau energy coefficients in the phase-field model. As shown in Fig. 4c, the polarization configuration at 500 K exhibits a labyrinthine state composed of elongated, meandering dipole assemblies, reminiscent of thermally triggered topological phase transitions reported in similar

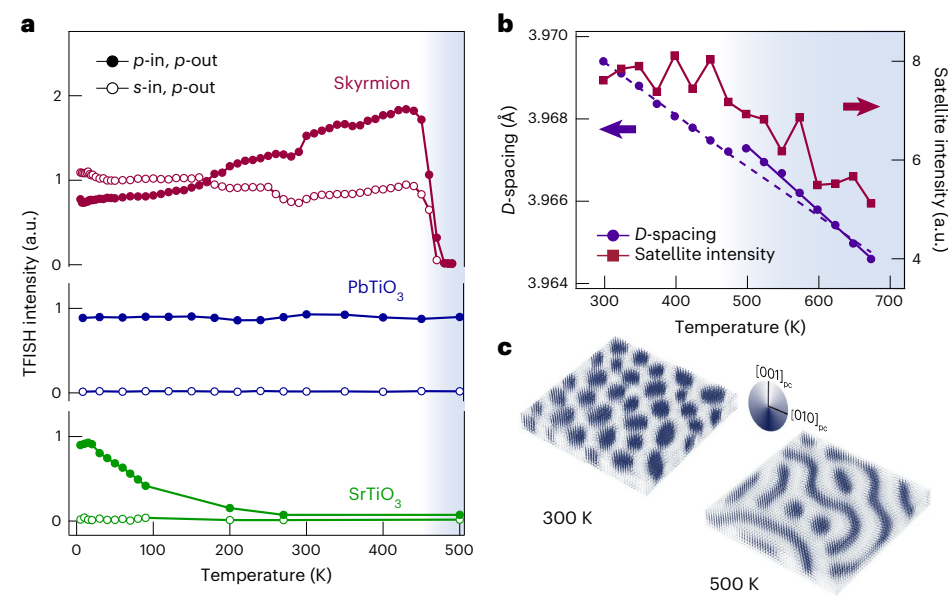


**Fig. 4** | **Temperature dependence of the terahertz-induced skyrmion dynamics. a**, Temperature evolution of the peak TFISH responses of the polar skyrmions, PbTiO<sub>3</sub> thin films and SrTiO<sub>3</sub> single crystals measured under the p-in/p-out and s-in/p-out conditions. **b**, Temperature-dependent X-ray diffraction results of (PbTiO<sub>3</sub>)<sub>16</sub>/(SrTiO<sub>3</sub>)<sub>16</sub> superlattices. The out-of-plane lattice parameters (d-spacing) are extracted from the  $\theta$ -2 $\theta$  scan patterns and the

satellite peak intensities associated with the in-plane periodicity are extracted from the  $\omega$ -rocking curves.  $\mathbf{c}$ , An illustration of the near-470 K structural transition obtained from phase-field simulations. Arrows represent the local polarization vectors within the PbTiO $_3$  layers. The blue shaded areas in  $\mathbf{a}$  and  $\mathbf{b}$  denote the high-temperature region corresponding to the labyrinthine state illustrated in  $\mathbf{c}$ .

material systems <sup>52,53</sup>. Although further microscopic validations are warranted (for example, using ultrafast X-ray scattering techniques), the simulations indicate that the observed structural transition at 470 K can substantially shift the frequencies of the collective modes of the skyrmions (Fig. 1b), leading to distinct dynamical behaviours. The TFISH responses, through either HRS or related SHG mechanisms, are thereby quenched due to a disrupted coupling between the superlattice with the terahertz field.

## Discussion

Polar skyrmions, as an energetically frustrated yet spatially ordered system, essentially comprise a continuum of frozen states along the structural evolution path of PbTiO<sub>3</sub>. The local polarization is fully developed at the skyrmion centres and highly suppressed near the walls, corresponding to local ferroelectric and paraelectric states, respectively. The paraelectric wall regions, known to stabilize steady-state negative capacitance<sup>7,8</sup>, underpin opportunities for exploiting their unique structural responses in future ultrafast control schemes. In terms of lattice dynamics, the continuum of states should encompass the temperature-dependent soft-mode dynamics of PbTiO<sub>3</sub>, which renormalizes into a set of resonant collective modes. The wall regions sustain considerable softening within the stability field of the skyrmions and thus are most susceptible to terahertz excitation. This characteristic originates from the topologically protected phase stabilities under a terahertz field and renders the broad temperature range for an effective excitation, unsupported by architype (incipient) ferroelectrics including PbTiO<sub>3</sub> and SrTiO<sub>3</sub>. The skyrmions are also dissimilar to chemically heterogenous materials with polar nanoregions, such as  $KTaO_3$  and  $Pb(Mg_{1/3}Nb_{2/3})O_3$  relaxors<sup>54–57</sup>. In the latter systems, dipolar relaxation dynamics is introduced by the randomly distributed polar nanoregions and moderately couples to terahertz fields at low temperatures. Furthermore, in the present case, the terahertz-induced transition is dominated by a strong collective mode at ~2.1 THz. This could potentially be tuned by modifying the superlattice structure or applying an external electric or stress field, by virtue of the structural robustness of the skyrmions.

In summary, we have observed the coherent excitations of the polar skyrmions driven by single-cycle terahertz pulses. Based on the TFISH/TKE measurements and dynamical phase-field simulations, we identify the connection between the spectrally complex macroscopic nonlinear optical responses with terahertz-excited collective modes of the skyrmions, highlighting the critical role of high-frequency collective modes in stabilizing the transient polar phase. The ultrafast dynamical behaviours of the skyrmions are stable against temperature, until they undergo a structural phase transition at ~470 K. The ability of terahertz-driven collective modes to trigger structural transitions enables dynamical reconfiguration of the functional states, with application prospects for neuromorphic computing by means of ultrafast analogue modulation of synaptic weights<sup>53,58</sup>. All these observations posit the skyrmions, and possibly also other topological polar systems, as a versatile platform for exploring rich ultrafast dynamical phenomena and engineering high-speed nonlinear optoelectronic functionalities.

#### Online content

Any methods, additional references, Nature Portfolio reporting summaries, source data, extended data, supplementary information, acknowledgements, peer review information; details of author contributions and competing interests; and statements of data and code availability are available at https://doi.org/10.1038/s41567-025-03056-8.

## References

- 1. Rusu, D. et al. Ferroelectric incommensurate spin crystals. *Nature* **602**, 240–244 (2022).
- Yadav, A. K. et al. Observation of polar vortices in oxide superlattices. Nature 530, 198–201 (2016).
- Junquera, J. et al. Topological phases in polar oxide nanostructures. Rev. Mod. Phys. 95, 025001 (2023).
- 4. Sun, Y. et al. Subunit cell-level measurement of polarization in an individual polar vortex. *Sci. Adv.* **5**, eaav4355 (2019).
- Wang, Y. J. et al. Polar meron lattice in strained oxide ferroelectrics. Nat. Mater. 19, 881–886 (2020).

- 6. Gong, F.-H. et al. Atomic mapping of periodic dipole waves in ferroelectric oxide. *Sci. Adv.* **7**, eabq5503 (2021).
- Yadav, A. K. et al. Spatially resolved steady-state negative capacitance. *Nature* 565, 468–471 (2019).
- Das, S. et al. Local negative permittivity and topological phase transition in polar skyrmions. Nat. Mater. 20, 194–201 (2021).
- Shao, Y.-T. et al. Emergent chirality in a polar meron to skyrmion phase transition. *Nat. Commun.* 14, 1355 (2023).
- Gómez-Ortiz, F., García-Fernández, P., López, J. M. & Junquera, J. Melting of crystals of polarization vortices and chiral phase transitions in oxide superlattices. *Phys. Rev. B* 105, L220103 (2022).
- Behera, P. et al. Electric field control of chirality. Sci. Adv. 8, eabj8030 (2022).
- Han, H. et al. Electric field-manipulated optical chirality in ferroelectric vortex domains. Adv. Mater. 36, 2408400 (2024).
- Stoica, V. A. et al. Optical creation of a supercrystal with three-dimensional nanoscale periodicity. *Nat. Mater.* 18, 377–383 (2019).
- Stoica, V. A. et al. Non-equilibrium pathways to emergent polar supertextures. *Nat. Mater.* 23, 1394–1401 (2024).
- Zhang, H. et al. Room-temperature skyrmion lattice in a layered magnet (Fe<sub>0.5</sub>Co<sub>0.5</sub>)<sub>5</sub>GeTe<sub>2</sub>. Sci. Adv. 8, eabm7103 (2022).
- Han, L. et al. High-density switchable skyrmion-like polar nanodomains integrated on silicon. *Nature* 603, 63–67 (2022).
- Yu, X. Z. et al. Real-space observation of a two-dimensional skyrmion crystal. Nature 465, 901–904 (2010).
- 18. Das, S. et al. Observation of room-temperature polar skyrmions. *Nature* **568**, 368–372 (2019).
- 19. Gong, F.-H. et al. Absence of critical thickness for polar skyrmions with breaking the Kittel's law. *Nat. Commun.* **14**, 3376 (2023).
- Damodaran, A. R. et al. Phase coexistence and electric-field control of toroidal order in oxide superlattices. *Nat. Mater.* 16, 1003–1009 (2017).
- Zhou, L. et al. Local manipulation and topological phase transitions of polar skyrmions. *Matter* 5, 1031–1041 (2022).
- Du, K. et al. Manipulating topological transformations of polar structures through real-time observation of the dynamic polarization evolution. *Nat. Commun.* 10, 4864 (2019).
- 23. Tan, C. et al. Engineering polar vortex from topologically trivial domain architecture. *Nat. Commun.* **12**, 4620 (2021).
- Li, M. et al. Electric-field control of the nucleation and motion of isolated three-fold polar vertices. Nat. Commun. 13, 6340 (2022).
- Li, X. et al. Atomic-scale observations of electrical and mechanical manipulation of topological polar flux closure. *Proc. Natl Acad. Sci. USA* 117, 18954–18961 (2020).
- 26. Li, Q. et al. Subterahertz collective dynamics of polar vortices. *Nature* **592**, 376–380 (2021).
- Cochard, C., Spielmann, T. & Granzow, T. Dielectric tunability of ferroelectric barium titanate at millimeter-wave frequencies. *Phys. Rev. B* 100, 184104 (2019).
- 28. Heide, C., Keathley, P. D. & Kling, M. F. Petahertz electronics. *Nat. Rev. Phys.* **6**, 648–662 (2024).
- 29. Hui, D. et al. Ultrafast optical switching and data encoding on synthesized light fields. Sci. Adv. 9, eadf1015 (2023).
- Wang, H. et al. Ultrafast excitation of polar skyrons. Preprint at https://doi.org/10.48550/arxiv.2505.09958 (2025).
- 31. Li, X. et al. Terahertz field-induced ferroelectricity in quantum paraelectric SrTiO<sub>3</sub>. Science **364**, 1079–1082 (2019).
- 32. Kozina, M. et al. Terahertz-driven phonon upconversion in  $SrTiO_3$ . Nat. Phys. **15**, 387–392 (2019).
- Chen, F. et al. Ultrafast terahertz gating of the polarization and giant nonlinear optical response in BiFeO<sub>3</sub> thin films. Adv. Mater. 27, 6371–6375 (2015).

- Chen, F. et al. Ultrafast terahertz-field-driven ionic response in ferroelectric BaTiO<sub>2</sub>. Phys. Rev. B 94, 180104 (2016).
- Nova, T. F., Disa, A. S., Fechner, M. & Cavalleri, A. Metastable ferroelectricity in optically strained SrTiO<sub>3</sub>. Science 364, 1075–1079 (2019).
- Miyamoto, T., Yada, H., Yamakawa, H. & Okamoto, H. Ultrafast modulation of polarization amplitude by terahertz fields in electronic-type organic ferroelectrics. *Nat. Commun.* 4, 2586 (2013).
- Qi, T., Shin, Y.-H., Yeh, K.-L., Nelson, K. A. & Rappe, A. M. Collective coherent control: synchronization of polarization in ferroelectric PbTiO<sub>3</sub> by shaped THz fields. *Phys. Rev. Lett.* **102**, 247603 (2009).
- 38. Linker, T. et al. Exploring far-from-equilibrium ultrafast polarization control in ferroelectric oxides with excited-state neural network quantum molecular dynamics. Sci. Adv. 8, eabk2625 (2022).
- 39. Burns, G. & Scott, B. A. Lattice modes in ferroelectric perovskites: PbTiO<sub>3</sub>. *Phys. Rev. B* **7**, 3088–3101 (1973).
- Mankowsky, R., Von Hoegen, A., Först, M. & Cavalleri, A. Ultrafast reversal of the ferroelectric polarization. *Phys. Rev. Lett.* 118, 197601 (2017).
- DiDomenico, M., Wemple, S. H., Porto, S. P. S. & Bauman, R. P. Raman spectrum of single-domain BaTiO<sub>3</sub>. Phys. Rev. 174, 522–530 (1968).
- 42. Ferguson, B. & Zhang, X.-C. Materials for terahertz science and technology. *Nat. Mater.* **1**, 26–33 (2002).
- 43. Peng, B., Hu, Y., Murakami, S., Zhang, T. & Monserrat, B. Topological phonons in oxide perovskites controlled by light. *Sci. Adv.* **6**, eabd1618 (2020).
- 44. Shin, D. et al. Simulating terahertz field-induced ferroelectricity in quantum paraelectric SrTiO<sub>3</sub>. *Phys. Rev. Lett.* **129**, 167401 (2022).
- 45. Wang, S. et al. Giant electric field-induced second harmonic generation in polar skyrmions. *Nat. Commun.* **15**, 1374 (2024).
- 46. Li, W. et al. Delineating complex ferroelectric domain structures via second harmonic generation spectral imaging. *J. Materiomics* **9**, 395–402 (2023).
- 47. Shi, J. et al. Revealing a distortive polar order buried in the Fermi sea. Sci. Adv. **10**, eadn0929 (2024).
- Chen, J., Han, P. & Zhang, X.-C. Terahertz-field-induced second-harmonic generation in a beta barium borate crystal and its application in terahertz detection. *Appl. Phys. Lett.* 95, 011118 (2009).
- 49. Cook, D. J., Chen, J. X., Morlino, E. A. & Hochstrasser, R. M. Terahertz-field-induced second-harmonic generation measurements of liquid dynamics. *Chem. Phys. Lett.* **309**, 221–228 (1999).
- 50. Lin, T. et al. Subwavelength, phase-sensitive microscopy of third-order nonlinearity in terahertz frequencies. *ACS Photon.* **11**, 33–41 (2024).
- Hoffmann, M. C., Brandt, N. C., Hwang, H. Y., Yeh, K.-L. & Nelson, K. A. Terahertz Kerr effect. Appl. Phys. Lett. 95, 231105 (2009).
- 52. Tong, P. et al. Thermal triggering for multi-state switching of polar topologies. *Nat. Phys.* **21**, 464–470 (2025).
- 53. Prosandeev, S. et al. Ultrafast activation and tuning of topological textures in ferroelectric nanostructures. *Adv. Elect. Mater.* **8**, 2200808 (2022).
- 54. Cheng, B., Kramer, P. L., Shen, Z.-X. & Hoffmann, M. C. Terahertz-driven local dipolar correlation in a quantum paraelectric. *Phys. Rev. Lett.* **130**, 126902 (2023).
- Li, X. et al. Terahertz pulse induced second harmonic generation and Kerr effect in the quantum paraelectric KTaO<sub>3</sub>. *Phys. Rev. B* 107, 064306 (2023).
- Prosandeev, S., Grollier, J., Talbayev, D., Dkhil, B. & Bellaiche, L. Ultrafast neuromorphic dynamics using hidden phases in the prototype of relaxor ferroelectrics. *Phys. Rev. Lett.* 126, 027602 (2021).

- 57. Park, S. et al. Light-driven ultrafast polarization manipulation in a relaxor ferroelectric. *Nano Lett.* **22**, 9275–9282 (2022).
- 58. Prosandeev, S. et al. Designing polar textures with ultrafast neuromorphic features from atomistic simulations. *Neuromorph. Comput. Eng.* **3**, 012002 (2023).

**Publisher's note** Springer Nature remains neutral with regard to jurisdictional claims in published maps and institutional affiliations.

Springer Nature or its licensor (e.g. a society or other partner) holds exclusive rights to this article under a publishing agreement with the author(s) or other rightsholder(s); author self-archiving of the accepted manuscript version of this article is solely governed by the terms of such publishing agreement and applicable law.

@ The Author(s), under exclusive licence to Springer Nature Limited 2025

#### Methods

#### Sample fabrication

 $[(PbTiO_3)_{16}/(SrTiO_3)_{16}]_8 \ superlattices \ were fabricated \ with \ reflection \ high-energy electron diffraction assisted pulsed laser deposition (Anhui Epitaxy Technology). (001)-cut (LaAlO_3)_{0.3} \cdot (SrAl_{0.5}Ta_{0.5}O_3)_{0.7} \cdot (LSAT) \ single \ crystals \ were used as substrates. PbTiO_3, SrTiO_3 \ and SrRuO_3 \ ceramic targets \ were ablated by a 248-nm KrF excimer laser (COMPex205, Coherent) \ with a fluence of 1.0 J cm^{-2}. The bottom electrode layer of SrRuO_3 \ was grown at 680 °C under 10-Pa oxygen pressure. A 6-nm-thick SrTiO_3 \ buffer layer, followed by a periodic sequence of PbTiO_3 \ and SrTiO_3 \ layers, was grown at 650 °C under 12-Pa oxygen pressure. Precise control of the unit-cell layer number was confirmed by reflection high-energy electron diffraction intensity oscillations. For the two control samples, single-layer PbTiO_3 thin films were grown at 700 °C under 12-Pa oxygen pressure using the same pulsed laser deposition equipment, and a commercial (001)-cut SrTiO_3 single crystal was used.$ 

#### Structural characterizations

Thin-film X-ray diffraction was carried out with a Malvern PANalytical Empyrean diffractometer employing Cu  $K_{\alpha l}$  radiation (wavelength: 1.5406 Å). The measurements included  $\theta$ –2 $\theta$  specular scans and  $\omega$ -rocking scans. The superlattice samples were placed in a vacuum chamber and heated from room temperature to 700 K. The lattice constants were calculated from the zero-order superlattice diffraction peak in the  $\theta$ –2 $\theta$  scan patterns. The satellite diffraction intensities were derived from the Gaussian fitting results of the satellite peaks near  $\omega$  = 21.5° and  $\omega$  = 24.1° in the rocking curves.

#### Ultrafast terahertz spectroscopies

A Ti:sapphire femtosecond laser amplifier (Spitfire Ace, Spectra-Physics) generated 35-fs pulses with a central wavelength of 800 nm, a repetition rate of 1 kHz and a single-pulse energy of 7 mJ. The 95% laser output was employed to generate terahertz radiation from a LiNbO<sub>3</sub> crystal by the tilted wavefront technique<sup>59</sup>. The terahertz radiation was focused onto the sample at normal incidence with the electric field along the [100] direction. The remaining weak laser output was used as a probe beam to generate either SHG or an optical Kerr signal from the sample. The probe pulses were focused on the sample surface at normal incidence, the 400-nm SHG light was collected in a near-backscattering direction and the Kerr signal was detected by a balanced detector. For the TFISH measurements, the polarization direction of the probe beam was controlled by a half-wave plate and formed an angle  $\alpha$  relative to the terahertz field, and a polarizer was used to select the SHG light with a polarization direction at an angle  $\varphi$  to the terahertz field. The SHG light was then delivered through several bandpass filters and detected using a photomultiplier tube. An optical chopper modulated the pump terahertz beam at 500 Hz. The measured signal was demodulated with the same frequency by a lock-in amplifier, ruling out static SHG signals that would generally exist in ferroelectric systems such as PbTiO<sub>3</sub>. A continuous-flow He cryostat with sapphire windows was used to vary the sample temperature from 4 K to 500 K. For the interferometric TFISH measurements, a  $\beta$ -BaB<sub>2</sub>O<sub>4</sub> (BBO) single crystal was put into the probe line to generate the local oscillator (LO) pulses collinearly in the orthogonal polarization direction. A calcite single crystal was used to compensate the optical path length difference between the probe and the LO light beams. A pair of fused-silica wedges (2.8°) served as the phase modulator and were adjusted with a piezoelectric displacement stage. Finally, the polarization direction of the probe and the LO beams were rotated to be parallel using a dual-wavelength waveplate. For the TKE measurements, the polarization direction of the probe beam was fixed at  $\alpha = 45^{\circ}$  relative to the terahertz field.

## Dynamical phase-field simulations

A phase-field model for the superlattice system was constructed to simulate the terahertz-induced ultrafast dynamics of the skyrmions based on a finite-element method solver (COMSOL Multiphysics). The model consisted of five periods of alternating PbTiO<sub>3</sub> and SrTiO<sub>3</sub> layers, each with a thickness of 6.4 nm (approximately 16 unit cells), atop a 10-nm substrate layer. Along the [100] and [010] directions, the model size was 50 × 50 nm² (approximately 125 × 125 unit cells). For the top and bottom (001) surfaces, short-circuit electrical boundary conditions were applied. For the two pairs of in-plane (100)/(010) surfaces, periodic boundary conditions were applied. At the bottom surface of the substrate, the mechanical displacements were fixed, corresponding to –1.2% biaxial strains induced by the lattice mismatch between PbTiO<sub>3</sub> and LSAT, whereas the top surface was mechanically free. The superlattice layers were assumed to be fully constrained to the substrate.

The free-energy functional F is defined in the form

$$F = \int (E_{land} + E_{elec} + E_{elas} + E_{grad}) dV$$
 (1)

where  $E_{\rm land}$ ,  $E_{\rm elec}$ ,  $E_{\rm elas}$  and  $E_{\rm grad}$  correspond to the Landau, electrostatic, mechanical and polarization gradient energy densities, respectively. In the model, these energetic terms were evaluated using three sets of field variables, including polarization (**P**), mechanical displacement (**u**) and electric potential ( $\varphi$ ). The spatiotemporal dynamics of the model are governed by a set of coupled equations of motion:

$$\mu \ddot{P}_i + \gamma \dot{P}_i = -\delta F / \delta P_i \tag{2}$$

$$\rho \ddot{u}_i + \beta \rho \dot{u}_i = -\delta F/\delta u_i \tag{3}$$

$$0 = -\delta F/\delta \varphi \tag{4}$$

where  $\mu, \gamma, \rho$  and  $\beta$  are the effective polarization mass density, polarization damping coefficient, mass density and elastic damping coefficient, respectively. Equation (2) is the second-order time-dependent Landau–Ginzburg–Devonshire equation, which determines the polarization dynamics, and equation (3) governs the elastodynamics. Equation (4) is Poisson's electrostatic equation, which neglects complex electrodynamics related to charge carrier transport, because the intrinsic carrier density is low in the skyrmion system and the terahertz excitation does not have large enough energy to populate free electron/hole carriers. For the superlattice layers, all three equations were employed, whereas for the substrate layer only equation (3) was enabled.

The steady-state configuration of the skyrmions was first obtained by setting both  $\mu$  and  $\rho$  to zero (thus nullifying the mass inertial effects) and evolving from small random initial polarization values (<0.0007 C m $^{-2}$ ) in the superlattice layers. For simulating terahertz excitation of the skyrmions, the  $\mu$  and  $\rho$  were turned on and the steady-state polarization configuration was set as the initial values. An additional electric field component was included in the equations, which had the same waveform as the electro-optic sampling results; subject to this virtual terahertz pulse, the evolution of the model was calculated within a time range of 0–40 ps. To best fit the experimentally observed TFISH response, the  $\mu$  was optimized to a value of 7.53  $\times$  10 $^{-18}$  kg m $^3$  A $^{-2}$  s $^{-2}$ . More details about the phase-field model can be found in ref. 26 and ref. 60.

#### Data availability

The experimental and simulation data presented in this article are available from the corresponding author upon request. Source data are provided with this paper.

### References

 Hebling, J., Yeh, K.-L., Hoffmann, M. C., Bartal, B. & Nelson, K. A. Generation of high-power terahertz pulses by tilted-pulse-front excitation and their application possibilities. J. Opt. Soc. Am. B 25, B6–B19 (2008). Li, Q. et al. Quantification of flexoelectricity in PbTiO<sub>3</sub>/SrTiO<sub>3</sub> superlattice polar vortices using machine learning and phase-field modeling. *Nat. Commun.* 8, 1468 (2017).

## **Acknowledgements**

This work was financially supported by the Basic Science Center Project of National Natural Science Foundation of China (NSFC) under grant no. 52388201 (Q.L., J.-F.L. and C.-W.N.), the Ministry of Education of China Scientific Research Innovation Capability Support Project for Young Faculty under grant no. ZYGXQNJSKYCXNLZCXM-M17 (Q.L.), NSFC grant nos. U24A2009 (Q.L.), 52150092 (Q.L.) and 11974414 (X.W.), the Beijing Municipal Natural Science Foundation under grant nos. JQ24011 (Q.L.) and Z240008 (Q.L.) and by the State Key Laboratory of New Ceramic Materials Research grant no. 2025QHTC-ZZKYB001 (J.-F.L.). A portion of this work was carried out at the Synergetic Extreme Condition User Facility (SECUF, https://cstr.cn/31123.02.SECUF).

### **Author contributions**

W.L. and X.W. performed the terahertz spectroscopies measurements. W.L., X.W., P.P. and J.L. developed the experimental set-up. S.W. fabricated the samples. W.L. and Q.L. performed the phase-field simulations. H.H. and J.M. performed the XRD measurements. J.-M.L.,

J.-F.L. and C.-W.N. discussed the results. W.L. and Q.L. wrote the paper with input from all the co-authors. Q.L. conceived of and supervised the project.

### **Competing interests**

The authors declare no competing interests.

#### **Additional information**

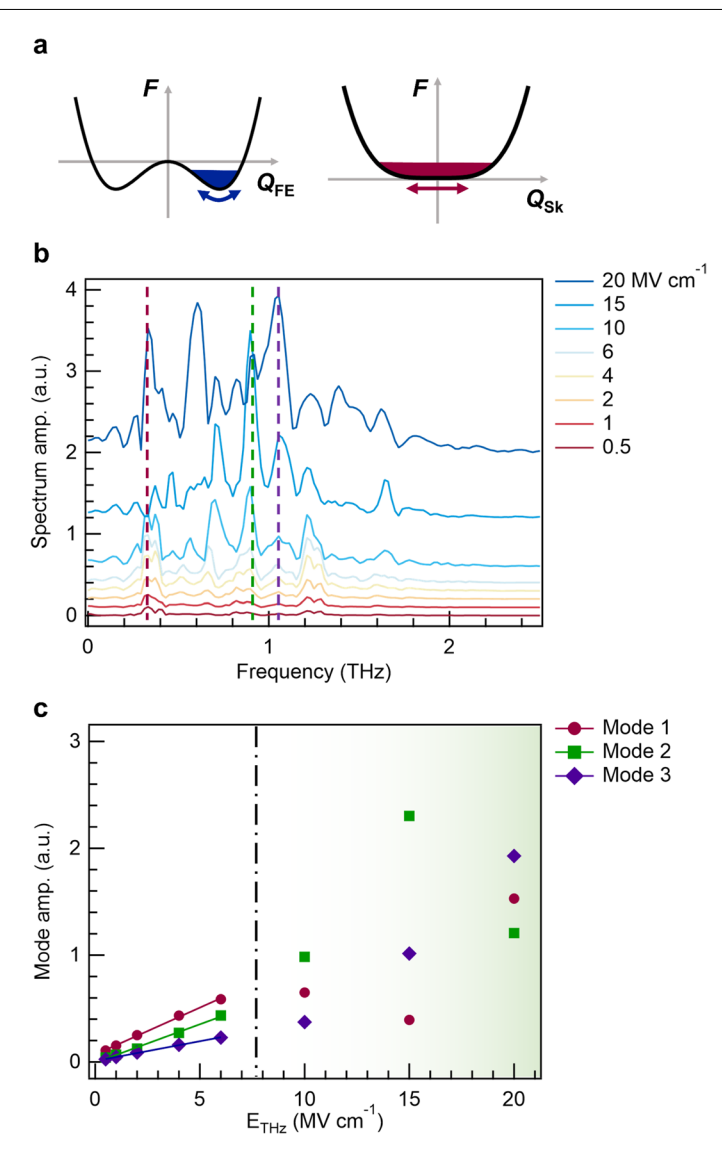
**Extended data** is available for this paper at https://doi.org/10.1038/s41567-025-03056-8.

**Supplementary information** The online version contains supplementary material available at https://doi.org/10.1038/s41567-025-03056-8.

**Correspondence and requests for materials** should be addressed to Xinbo Wang or Qian Li.

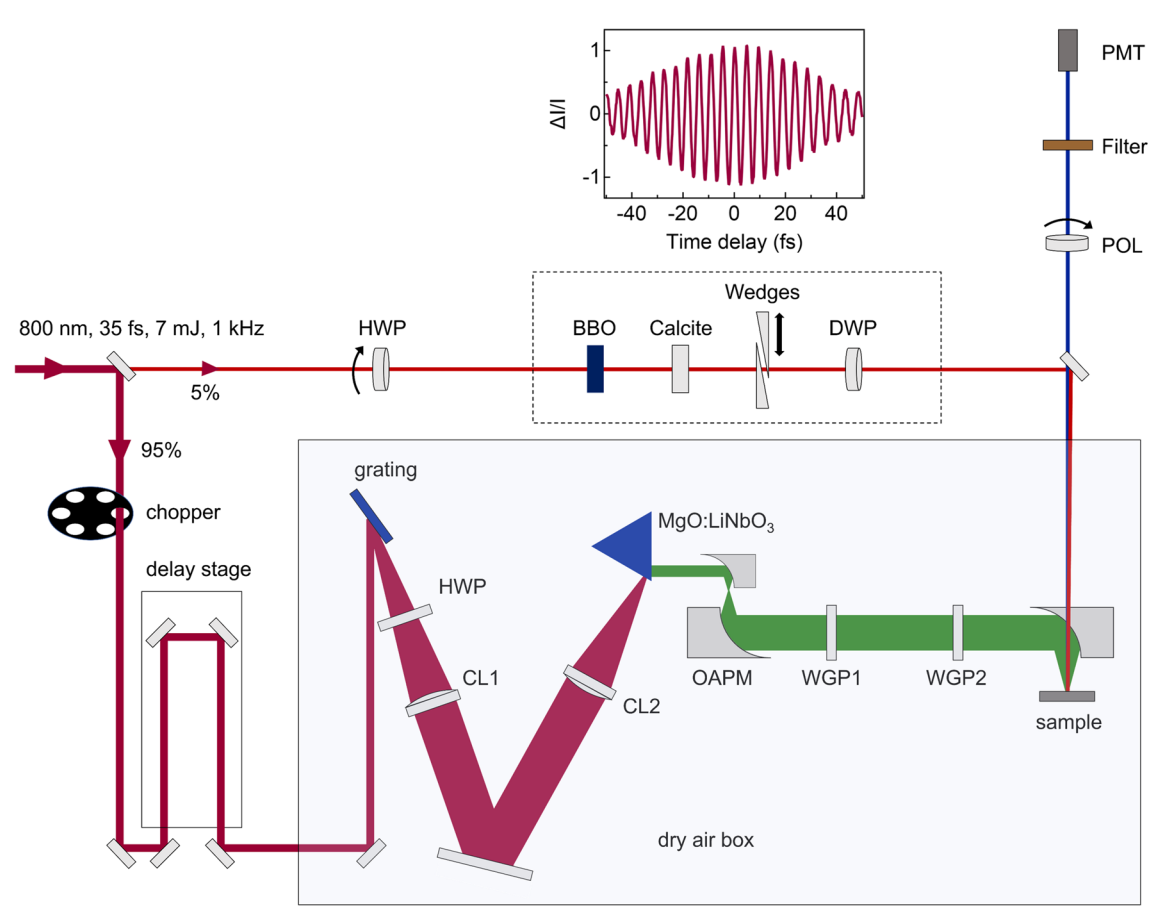
**Peer review information** *Nature Physics* thanks Brahim Dkhil and the other, anonymous, reviewer(s) for their contribution to the peer review of this work.

**Reprints and permissions information** is available at www.nature.com/reprints.



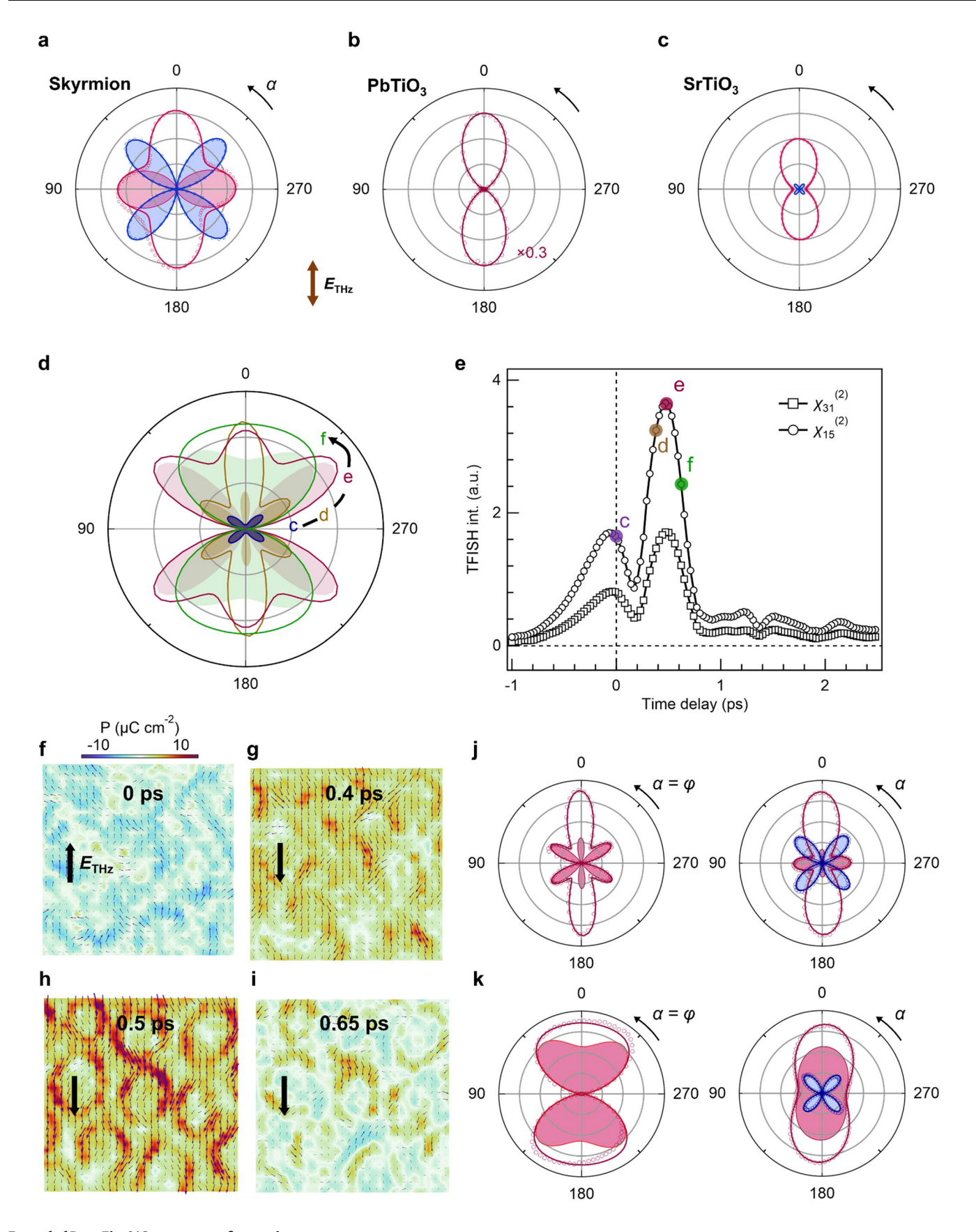
Extended Data Fig. 1 | Schematic of the free-energy landscapes and phase-field simulations of the mode nonlinearity for skyrmions. a The free-energy landscapes for PbTiO $_3$  soft mode and the skyrmion collective modes. b Fourier-transformed spectra of the simulated TFISH responses of polar skyrmion at various THz field

strengths. **c** THz-field dependence of the amplitude of the collective modes. The modes with frequencies of approximately 0.35 THz, 0.9 THz and 1.05 THz are colored in red, green and violet, respectively, as marked in (**b**). The nonlinearity region starts at -6 MV cm<sup>-1</sup>, well above the experimental THz-field strength (-1 MV cm<sup>-1</sup>).



 $\label{lem:extended} \textbf{Data Fig. 2} | Schematic illustration of the TFISH experiment setup. An illustration of the TFISH experiment setup. HWP: half-wave plate; QWP: quarter-wave plate; DWP: dual-wavelength waveplate; CL: plano-convex cylindrical lens; OAPM: off-axis parabolic mirror; WGP: terahertz wire grid polarizer; PMT: photomultiplier$ 

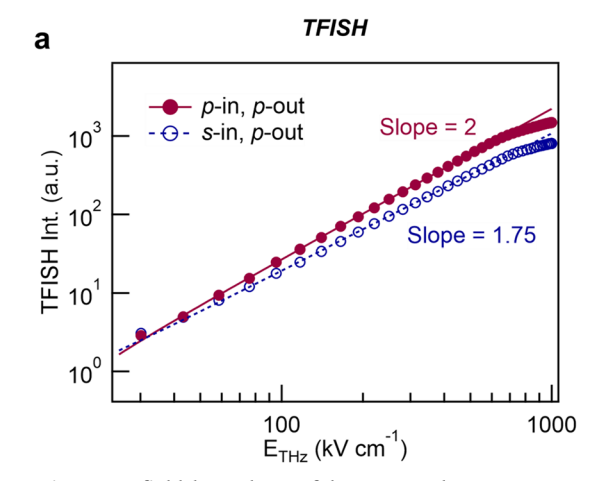
tube. The interference (i-) TFISH signal as a function of time delay between the TFISH response and BBO-crystal local oscillator (LO) is adjusted by a pair of fused-silica wedges. The top inset is an example of measured iTFISH patterns.

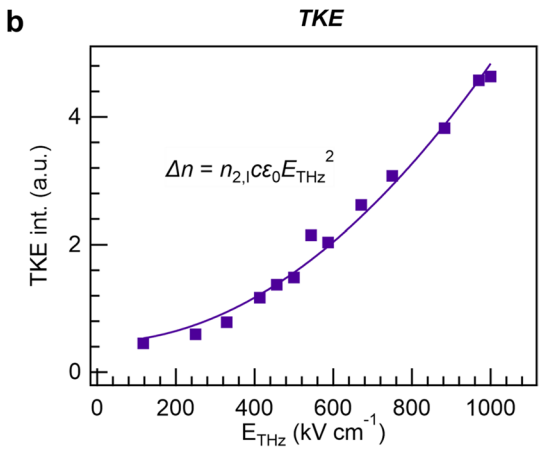


 $\textbf{Extended Data Fig. 3} \,|\, \textbf{See next page for caption.}$ 

Extended Data Fig. 3 | TFISH polarimetry measured under different conditions and the related structural evolutions by phase-field simulation. a–c TFISH  $\alpha$ -scan polarimetry patterns at the peak around 0.6 ps time delay in main text Fig. 2b for (a) the polar skyrmions, (b) the PbTiO $_3$  thin film and (c) SrTiO $_3$  single crystal, respectively. The data was measured by rotating incident angle  $\alpha$  while fixing  $\varphi$  at 0° (red) and 90° (blue). d TFISH  $\alpha/\varphi$ -coupled polarimetry patterns at selected delay times, as marked in (e). The data was measured by rotating  $\alpha$  and  $\varphi$  in parallel. e

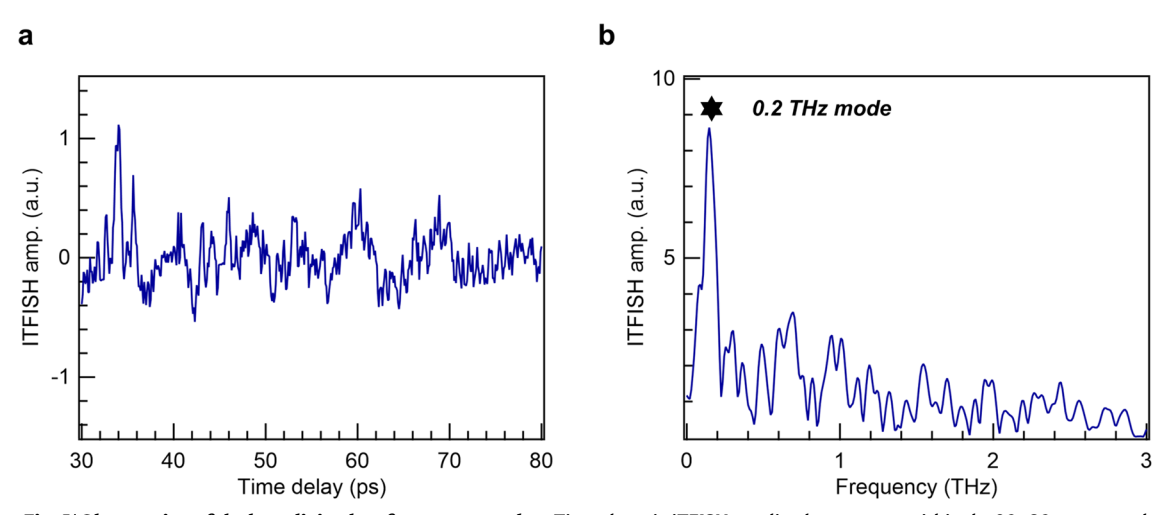
Model fitting results of the  $\chi^{(2)}$  contribution using the equation in Supplementary Note 1. Similar behaviors were seen for both  $\chi_{3i}$  and  $\chi_{15}$ , showing two intensity peaks related to the rise and fall of the polar order within the skyrmions and no oscillation behavior.  $\mathbf{f}$ - $\mathbf{i}$  (001)-plane slices of the polarization configurations of the skyrmions obtained from dynamical phase-field simulations.  $\mathbf{j}$ ,  $\mathbf{k}$  TFISH polarimetry patterns at ( $\mathbf{j}$ ) 0.4 ps and ( $\mathbf{k}$ ) 0.65 ps corresponding to the time delays in ( $\mathbf{g}$ ) and ( $\mathbf{i}$ ), respectively. Left:  $\alpha/\varphi$ -coupled scan results. Right:  $\alpha$ -scan results.



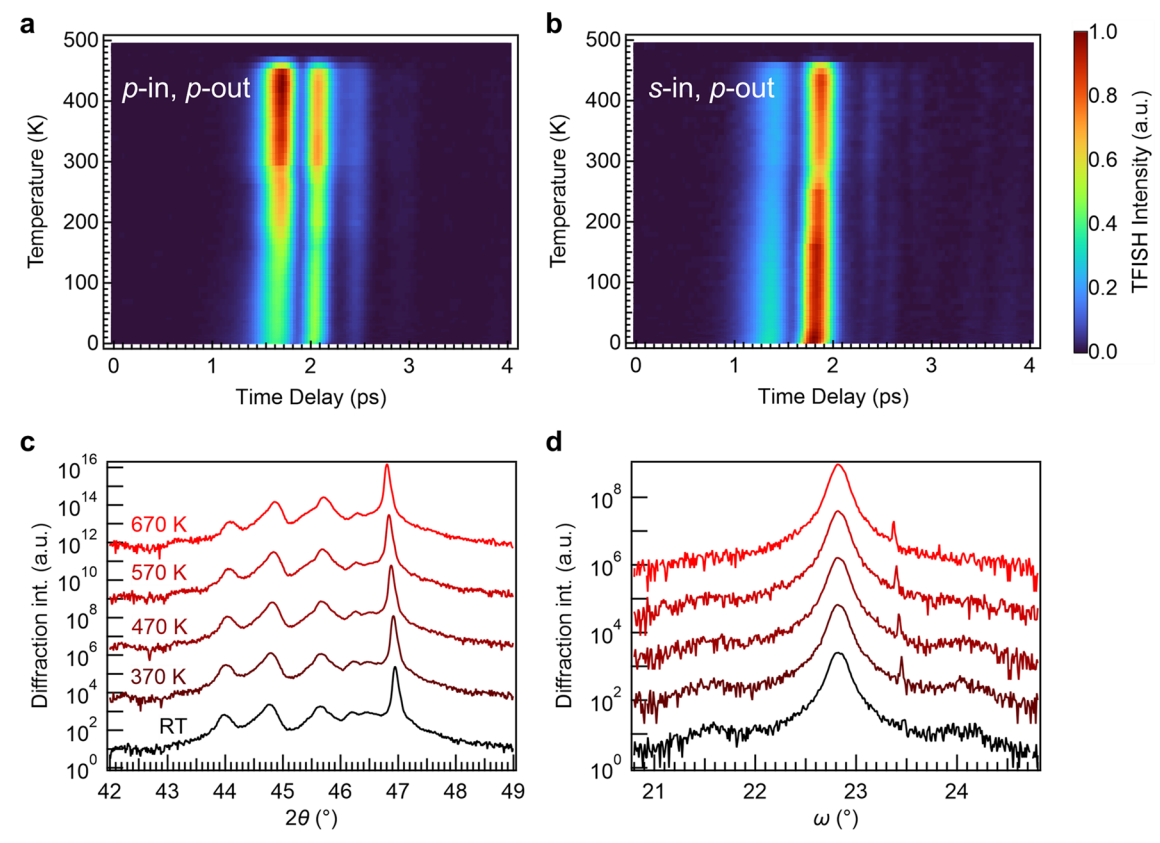


**Extended Data Fig. 4** | **THz-field dependence of the TFISH and TKE responses.** THz-field dependence of (**a**) the TFISH and (**b**) the TKE responses of the polar skyrmions along with power-function fitting results. The TFISH results are shown in

the double-logarithmic scales for clarity. The TKE dependence trace is well fitted with a quadratic function corresponding to the second-order nonlinear refractive index relationship.



 $\textbf{Extended Data Fig. 5} | \textbf{Observation of the long-living low-frequency mode. a} \ \text{Time-domain iTFISH amplitude} \ \text{spectrum within the 30-80 ps range, showing multiple} \ \text{weak oscillations. b} \ \text{Fourier-transformed spectrum of (a) showing a well-defined 0.2 THz oscillation mode in line with the 0-6 ps data in the main text Fig. 3.}$ 



**Extended Data Fig. 6** | **Temperature evolution of the TFISH time-domain spectra and X-ray diffraction patterns. a**, **b** Temperature evolution of the TFISH time-domain spectra under the (**a**) p-in/p-out and (**b**) s-in/p-out conditions, showing minimal changes in the mode frequencies followed by a sudden quench of the intensities at 470 K. **c**, **d** X-ray diffraction patterns for (PbTiO<sub>3</sub>)<sub>16</sub>/(SrTiO<sub>3</sub>)<sub>16</sub>

superlattices measured at different temperatures using (c)  $\theta$ - $2\theta$  and (d)  $\omega$ -rocking scan modes. The satellite peak intensities near  $\omega$  = 21.5° and  $\omega$  = 24.1° decreased with increasing temperature but did not completely varnish across the measured temperature range.